Physics of Plasmas

# Knock-on deuteron imaging for diagnosing the morphology of an ICF implosion at OMEGA

Cite as: Phys. Plasmas **29**, 072711 (2022); https://doi.org/10.1063/5.0096786
Submitted: 21 April 2022 • Accepted: 01 July 2022 • Published Online: 20 July 2022
Published open access through an agreement with Massachusetts Institute of Technology

J. H. Kunimune, H. G. Rinderknecht, P. J. Adrian, et al.

Physics of Plasmas ARTICLE scitation.org/journal/php

# Knock-on deuteron imaging for diagnosing the morphology of an ICF implosion at OMEGA

Cite as: Phys. Plasmas **29**, 072711 (2022); doi: 10.1063/5.0096786
Submitted: 21 April 2022 · Accepted: 1 July 2022 ·
Published Online: 20 July 2022



J. H. Kunimune,[1,a)] H. G. Rinderknecht,[2] P. J. Adrian,[1] P. V. Heuer,[2] S. P. Regan,[2] F. H. Séguin,[1] M. Gatu Johnson,[1] R. P. Bahukutumbi,[2] J. P. Knauer,[2] B. L. Bachmann,[3] and J. A. Frenje[1]

## AFFILIATIONS

[1]MIT PSFC, Cambridge, Massachusetts 02139, USA
[2]LLE, Rochester, New York 14623, USA
[3]LLNL, Livermore, California 94550, USA

[a)]Author to whom correspondence should be addressed: kunimune@mit.edu

## ABSTRACT

Knock-on deuteron imaging is a new diagnostic technique that is being implemented at the OMEGA laser facility to diagnose the morphology of an inertial confinement fusion (ICF) implosion. It utilizes the fact that some of the neutrons from deuterium–tritium (DT)-fusion reactions generated in the central hot-spot of an ICF implosion elastically scatter deuterons as they traverse the surrounding shell layer. The energy of these "knock-on" deuterons depends on the scattering angle, where the most energetic deuterons are forward-scattered and probe the shape of the central hot-spot, while lower-energy deuterons are made by side-scattering or slowing down in the fuel and carry information about the distribution of the dense DT-fuel layer surrounding the hot-spot. The first proof-of-concept tests have been conducted successfully. In these tests, three penumbral imagers with different views on an implosion recorded deuterons scattered from the dense shell of DT-gas-filled deuterated plastic shell implosions with prescribed offsets. Data from these experiments are presented here, along with novel analysis techniques that iteratively reconstruct the deuteron source from the data. Reconstructed hot-spot and shell radii agree with 1D hydro simulations and indicate a P1 asymmetry in the direction of the offset. A comparison of coaxial deuteron and x-ray images suggests the presence of a mix between the hot-spot and shell on the order of 15 $\mu$m. This new diagnostic capability will allow us to study asymmetries in unprecedented detail at OMEGA.



## I. INTRODUCTION

Inertial confinement fusion (ICF) involves a spherical capsule that is filled with deuterium–tritium (DT) fuel in the form of gas at vapor pressure surrounded by a cryogenic ice layer inside an ablator.[1] In the case of laser direct drive hot-spot ignition, as is studied at the OMEGA laser facility,[2] the energy from a laser is directly delivered to the ablator, which causes the outer part of it to heat up and expand outward. When the outer part of the ablator expands, the remaining inner part implodes to conserve momentum. At peak compression, the DT-fuel is nearly isobaric and composed of a hot central plasma called the hot-spot, containing a small fraction of the fuel, and a surrounding colder fuel-shell layer, where the latter can be divided into a stagnated high-density region on the inside and a trailing fuel mass region on the outside that is still converging. For optimal performance, the hot-spot and high-density fuel must be spherical, and they must have the highest possible ion temperature $T_i$ and areal density $\rho R$ (defined as $\int_0^\infty \rho dr$), respectively. While the national ICF program has made significant progress,[3] improving the implosion performance toward ignition conditions remains its primary goal.

There are several reasons that ignition remains challenging to achieve. One of the most significant ones is low-mode asymmetries in the fuel—in particular modes described by spherical harmonics $l = 1$ and $l = 2$ (P1 and P2)—that are caused by a combination of laser-drive asymmetry and engineering features on the capsule.[4–7] As the implosion converges, these asymmetries are amplified and generate complex geometries and substantial plasma flows.[8] This prevents efficient conversion of implosion kinetic energy to hot-spot thermal energy, which leads to a lower $T_i$ in the hot-spot, lower $\rho R$ in the high-density fuel, and shorter confinement time.[9–11]

Despite the significant impact that fuel $\rho R$ asymmetries have on the implosion performance, no diagnostics currently exist on OMEGA to measure them in great detail. X-ray imaging diagnostics have been

developed to diagnose hot-spot asymmetries,[12,13] but these are not sensitive to asymmetries in the dense fuel. Low-mode asymmetries in both the hot-spot and shell can be determined by comparing ion-temperature, flow velocity, and $\rho R$ measured in different directions via neutron spectrometry[14,15] or knock-on charged-particle spectrometry.[16–18] However, the number of degrees of freedom with which the asymmetry can be inferred is limited by the number of spectrometers positioned around the implosion. For that reason, current capabilities mainly diagnose the oblateness or prolateness of an implosion and cannot measure the precise direction and magnitude of higher-mode asymmetries.

At the National Ignition Facility (NIF),[19] the real-time neutron activation diagnostics are used to measure relative $\rho R$ on 48 lines of sight, and the neutron imaging system is used to capture primary and downscattered neutron images.[20,21,46] This is not feasible at OMEGA; however, because the magnitude of $\rho R$ is lower, meaning that neutron activation diagnostics would have unacceptably high statistical uncertainties, and the neutron yield is lower, meaning that neutron imaging is not efficient enough to provide high-quality downscattered images.

To address these issues, a diagnostic method to probe the three-dimensional (3D) implosion geometry is needed that does not require an unrealistic number of spectrometers, high yields, or a high $\rho R$. Knock-on deuteron imaging (KODI) is a new diagnostic technique currently being implemented on OMEGA, which will be used to diagnose the 3D geometry of both the hot-spot and surrounding high-density fuel of an ICF implosion.[43]

This paper is structured as follows: Sec. II describes the principle and hardware of the diagnostic. Section III describes commissioning experiments for the system. Section IV discusses the data-reconstruction algorithms. Section V presents reconstructions from the commissioning experiments. Section VI discusses conclusions and the path forward, and Sec. VII summarizes and closes.

## II. THE KODI ON THE OMEGA LASER FACILITY

### A. The principle of the KODI technique

The KODI technique utilizes the fact that some of the neutrons from DT fusion reactions generated in the central hot-spot of an ICF implosion elastically scatter off deuterons as they traverse the surrounding DT plasma. In a typical implosion at OMEGA ($\rho R = 100\,\mathrm{mg/cm^2}$), about 1% of DT neutrons generate "knock-on" deuterons, mostly in the dense fuel. The energy of a knock-on deuteron depends on the scattering angle [$E_\mathrm{d} = \frac{8}{9} E_\mathrm{n} \cos^2(\theta)$]. As illustrated in Fig. 1, a high-energy deuteron is scattered in approximately the same direction as that of the incoming 14 MeV neutron. This means that an image of the high-energy deuteron emission is approximately equivalent to an image of the 14 MeV neutron emission or an image of the hot-spot. The accuracy of this approximation depends on the minimum accepted deuteron energy (for 9 MeV deuterons, the scattering angle is 32°, which broadens the source radius by about 10%), as shown in Fig. 2. In contrast, a low-energy deuteron is either scattered at a large angle or born at higher energy and then slowed down by passing through the fuel. This means that an image of the low-energy deuteron emission contains information about the distribution of fuel mass around the hot-spot and has a radial extent similar to the radius of the dense fuel. The low-energy deuteron image is not exactly the same as an image of the fuel mass but must be interpreted to reconstruct the fuel morphology.

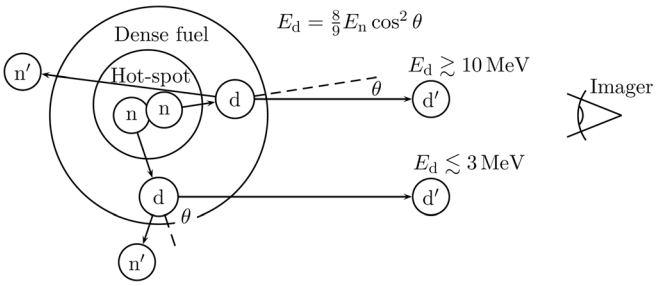


**FIG. 1.** A cartoon depicting the generation of knock-on deuterons in an implosion. The birth energy of a deuteron $E_\mathrm{d}$ is determined by the energy of the incoming neutron $E_\mathrm{n}$ and the scattering angle $\theta$ between the neutron and the deuteron. Due to stopping in the fuel, its energy at the detector also depends on the $\rho L$ of plasma that it passes through before leaving the implosion. As discussed in the text, forward-scattered high-energy deuterons provide an image of the neutron-producing hot-spot, and side-scattered low-energy deuterons provide information about the high-density fuel surrounding the hot-spot.

The deuteron images are recorded using charged-particle penumbral imaging. This is a form of coded aperture imaging that uses circular apertures that are larger than the typical source size.[22] The resulting image is composed of a large circular region of uniform intensity surrounded by a thin region of varying intensity called the penumbra. An example of a penumbral image is shown in Fig. 3. The size and shape of the source are encoded in the penumbra and can be extracted using a reconstruction technique. While the interpretation of a penumbral image is more complicated than that of a pinhole image, penumbral apertures provide better statistics than pinholes do. Penumbral imaging has been used extensively to image proton and alpha particle emission from ICF implosions[23–25] but has never before been applied to knock-on deuterons.

As a single deuteron image is only two-dimensional, one imager is insufficient to fully characterize the 3D morphology of the implosion. To obtain detailed information about fuel asymmetries, their causes, and their impact on the implosion performance, multiple imagers must be fielded along nearly orthogonal lines of sight. At least three such imagers are needed for the 3D reconstruction of the hot spot; additional imagers will be required to improve the 3D reconstruction of the shell.

### B. The KODI hardware

To image knock-on deuterons in the commissioning experiments, we used the hardware of the existing imaging system shown in Fig. 4.[23] Each imager consists of a 2 mm diameter penumbral aperture positioned about 4.2 cm from the implosion and a CR-39/image-plate detector package positioned about 63 cm from the implosion, for a magnification of $M = 15$.

The CR-39 detector is a piece of plastic in which deuterons generate a trail of chemical damage, which can be made visible under a microscope by etching the CR-39 for about six hours in sodium hydroxide.[26,27] Because the diameter of a track depends on the stopping power $\frac{\mathrm{d}E}{\mathrm{d}x}$ of the deuteron as it passes through the CR-39, energy-resolved deuteron images can be obtained by binning the deuteron track distribution by diameter. Figure 5 shows a typical relationship between track diameter and deuteron energy.[28] Because high-energy

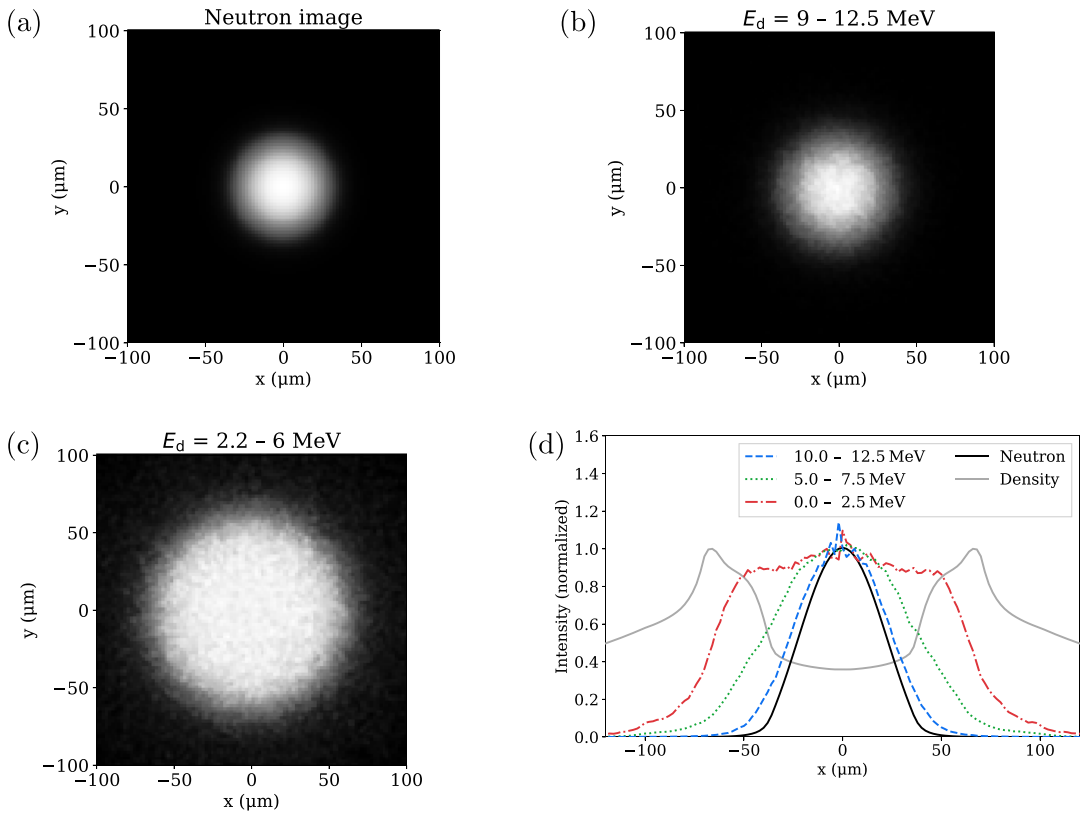


**FIG. 2.** Synthetic neutron and knock-on deuteron images for a DT-gas-filled CD-shell implosion to illustrate the KODI technique. The results from a 1D hydrodynamic simulation of the implosion were used as an input for the generation of these images. (a) Synthetic 14 MeV neutron source from the simulated implosion. Neutrons exclusively come from the hot-spot (core of the implosion). (b) Synthetic high-energy deuteron source in the range of 9–12.5 MeV (14 MeV neutrons generate knock-on deuterons with a maximum of 12.5 MeV). It is similar in size and shape to the neutron source and, thus, provides information about the hot-spot size. (c) Synthetic low-energy deuteron source in the range of 2.2–6 MeV. It extends to the outside of the dense shell that surrounds the hot-spot and, thus, provides information about the shell morphology. (d) Lineout of the 14 MeV neutron source distribution contrasted with lineouts of the deuteron source in several energy bins. The neutron and high-energy deuteron sources have nearly the same width, while the low-energy sources extend into the surrounding shell. The normalized burn-averaged density profile is shown in gray for reference.

deuterons image the hot-spot and low-energy deuterons provide information about the shell, this energy resolution allows us to separate information about different parts of the implosion. CR-39 is also sensitive to fusion neutrons, with a sensitivity that ranges from $2 \times 10^{-5}$ to $1 \times 10^{-4}$.[29] However, because neutrons do not interact with the aperture, this only results in a small uniform background that is subtracted in the analysis.

To obtain 3D information about the implosion morphology, three deuteron imagers were fielded with three nearly orthogonal lines of sight, at angles between 79° and 10° from each other. The complete imager configuration in relation to the OMEGA target chamber is shown in Fig. 6.

## III. EXPERIMENTS AND RESULTING DATA

Two sets of KODI commissioning experiments were conducted on October 10, 2019 and June 25, 2020. In these experiments, warm DT-gas-filled deuterated-plastic (CD) capsules were imploded at OMEGA. While KODI is intended to image cryogenic DT-implosions, warm plastic shell implosions are simpler to execute, and the deuterium areal density of a CD shell mimics that of the DT-ice layer in a cryogenic implosion.

Twelve shots were performed in total. Nine used 20 $\mu$m thick CD shells, while the remaining three had 27 $\mu$m shells. All twelve were filled with 18 atm DT gas to an inner diameter of 860 $\mu$m, as shown in Fig. 7, and driven by a 27 kJ, 1 ns square pulse. The achieved neutron yield and $\rho R$ of each shot are given in Table I.

The goal of these experiments was to demonstrate that fuel asymmetry can be inferred from deuteron images and to provide test data for the reconstruction algorithms. To this end, some of the capsules were initially offset from the target chamber center (TCC) by 40 $\mu$m or 80 $\mu$m to induce P1 drive asymmetry in a known direction.

KODI was fielded on three lines of sight with tungsten apertures of radius 1 mm. Each line of sight used 15–25 $\mu$m of aluminum or tantalum filtering in front of CR-39 (to optimize the detection of deuterons and protect against high-energy ablator ions) and 250 $\mu$m of aluminum between CR-39 and image plates (to further attenuate the x-ray fluence and to stop any protons scattered in the CR-39 in front).

An example from the collected KODI data is shown in Fig. 8. A few unexpected effects are apparent in these data. One was large-scale

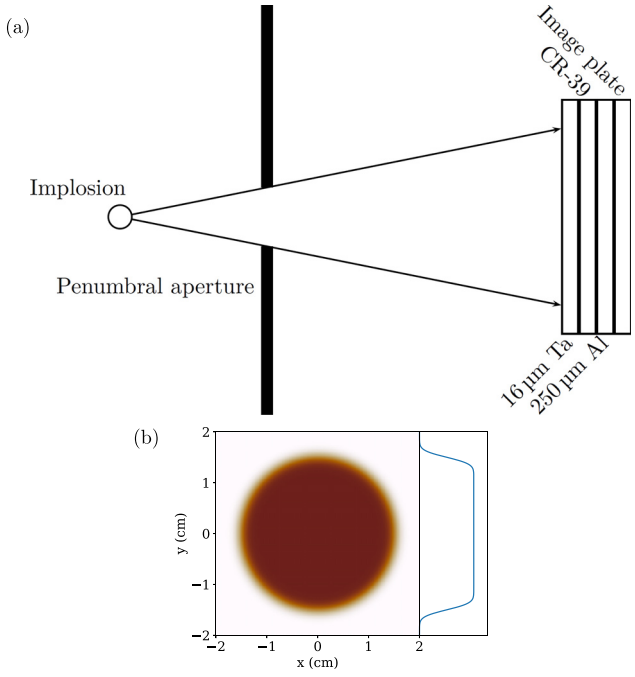


**FIG. 3.** Charged-particle penumbral imaging system for imaging knock-on deuterons in space and energy. (a) Schematic of a typical penumbral imaging hardware. Deuterons emitted from the implosion pass through a penumbral aperture, which is much larger than the source of deuterons. Accepted deuterons are subsequently measured by a detector. (b) A typical penumbral image, along with a lineout through the center. The information about the source is distributed across the region of varying intensity in the penumbra.

non-radially symmetric variations in the track-density throughout the center of the image. These variations appear in different directions and with different magnitudes on each image. They could be caused by non-radial variations in the electric field in the aperture or implosion corona, or nonuniformities in the CR-39 sensitivity. Despite this, the number of deuteron tracks counted was within 10% of the expected value based on the measured DT-neutron yield.

In addition, a rounded "shoulder" region of reduced track-density was consistently observed in the region just inside the penumbra, which should be uniform. This is attributed to aperture charging.

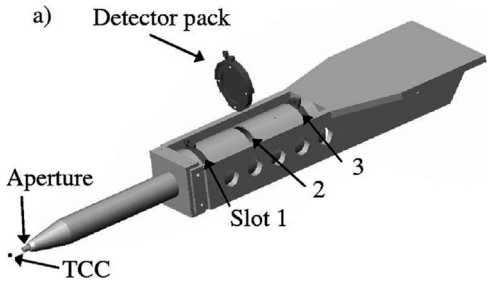


**FIG. 4.** CAD drawing of the hardware used in the KODI commissioning experiments. The aperture and CR-39 detector are positioned about 4.2 and 63 cm away from the implosion at the target chamber center (TCC), respectively, for a magnification of $M = 15$.

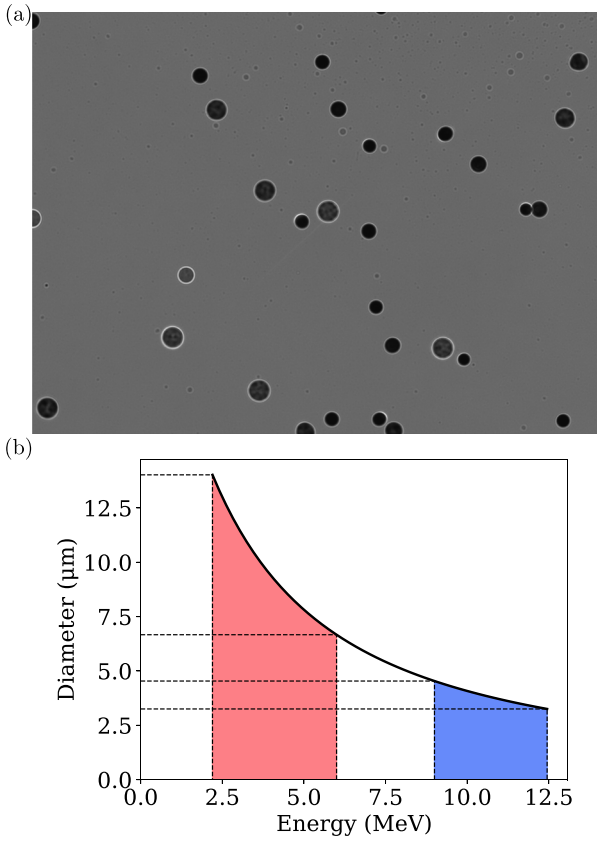


**FIG. 5.** CR-39 deuteron track data. (a) One microscope frame of a piece of CR-39 that has been exposed to charged particles with different energies. The piece of CR-39 has been etched for 5 h in 80 °C NaOK to widen the particle trails of damage to large dark circular tracks that are visible under a microscope. The region shown is $429.6 \times 314.5\ \mu m^2$. (b) Typical relationship between deuteron track diameter and deuteron energy in a piece of CR-39 that has been etched for 5 h.[28] The colored regions indicate the energy cuts typically used for the analysis of the KODI data.

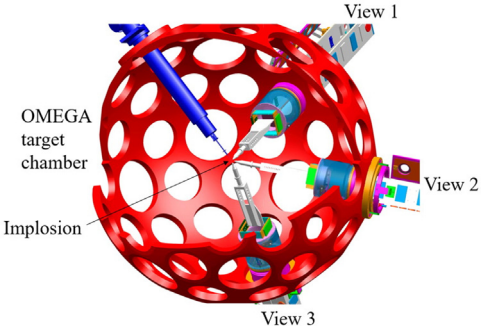


**FIG. 6.** CAD drawing of KODI on the OMEGA target chamber with nearly orthogonal lines of sight to the implosion. Each system is fielded in one of the OMEGA ten-inch manipulators (TIM).

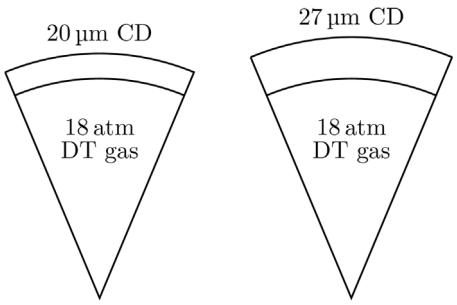


**FIG. 7.** The two capsule designs used in the KODI commissioning experiments.

The imaging aperture seems to build up a negative electric charge either from currents in the hardware that is induced by the electromagnetic pulse from the implosion or from electrons that are ejected from the implosion early in time and collide with the aperture. This deflects the trajectories of deuterons that pass through it, distorting the point-spread function. The resulting image becomes larger, the penumbra becomes wider, and the particle fluence just inside the penumbra is depleted in a manner consistent with what was observed in these experiments. The degree of aperture charging varied between shots and between lines of sight. This effect must be accounted for in the analysis or minimized, if not avoided, in the experiment.

## IV. DATA ANALYSIS METHODOLOGY

The recorded KODI image is the convolution of the knock-on deuteron source and instrument point-spread function. The source must be inferred from this projection before it can be interpreted. Although numerous reconstruction techniques exist for penumbral imaging,[23,30–32,45,47] the general iterative signal recovery technique given by Gelfgat *et al.* (GKP)[33] is used in this work. For the KODI data, it is reasonably robust to noise even though the signal is sometimes weak and allows for point-spread functions of arbitrary shape, as discussed in Sec. IV A.

The GKP technique takes a vector of $n$ whole number signal measurements $\{F_i\}$ and a linear response matrix $\{P_{ik}\}$ and finds the vector of $m$ non-negative inferred source values $\{G_k\}$ that produces the model $\{S_i\}$ that best matches the measurements, where

$$S_i = \sum_{l=1}^{m} P_{il} G_l. \tag{1}$$

In the case of KODI, the measurement vector $\{F_i\}$ represents the number of deuteron tracks in each pixel of the penumbral image, the source vector $\{G_k\}$ represents the emission in each pixel of the source, and the response matrix $\{P_{ik}\}$ represents the point-spread function that relates them—the value of $P_{ik}$ is the fraction of the deuterons from source pixel $k$ that makes it through the aperture and land in penumbral image pixel $i$. In addition, KODI data include a uniform background that comes from a combination of neutron and charged-particle scattering in the aperture and detector. To account for this in the reconstruction, an additional element $G_0$ must be added to the source vector, along with a corresponding row in the transfer matrix where $P_{i0} = 1$.

The GKP algorithm iterates on a guess of $\{G_k\}$, by convolving it with $\{P_{ik}\}$ and comparing the resulting synthetic data to $\{F_i\}$. The specific expressions used for this process cause the guesses to converge such that the likelihood of the observed data $\mathcal{L}$, assuming that each value of $\{F_i\}$ is drawn from a Poisson distribution, is maximized,

$$\mathcal{L} = \prod_{j=1}^{n} \left( \frac{e^{-S_j} S_j^{F_j}}{F_j!} \right). \tag{2}$$

This finds the solutions that best explain the data. Note that for a fixed $F_j$, $\mathcal{L}$ is maximized by $S_j = F_j$. However, because maximizing $\mathcal{L}$ usually means overfitting, the algorithm must be terminated after a finite number of iterations. Gelfgat *et al.* recommend terminating once $\chi^2 \equiv \sum_{j=1}^{n} (F_j - S_j)^2 / S_j$ goes below a predefined threshold value $\chi^2_P$. However, KODI data often have artifacts that raise the value of $\chi^2$ over its theoretical limit by 10% or more, so finding the value of $\chi^2_P$ that fits the image without overfitting it is quite difficult. Instead,

**TABLE I.** A summary of the KODI commissioning experiments. KODI images were captured in the three nearly orthogonal lines of sight. Targets were intentionally offset from the target chamber center toward one of the KODI systems; the precise magnitude of the offset was measured at shot time using high-speed video cameras. The high-energy knock-on deuteron yields and $\rho R$s at bang time were inferred using the charged-particle spectrometer.[16]

| Shot No. | Shell ($\mu$m) | Offset ($\mu$m) | Filter ($\mu$m) | DT-n yield | Deuteron yield | $\rho R$ (mg/cm$^2$) |
|---|---|---|---|---|---|---|
| 95 519 | 20 | 1.0 | 25 Al | $1.1 \times 10^{13}$ | $2.4 \times 10^{9}$ | 41 |
| 95 520 | 20 | 39.9 | 16 Ta | $1.2 \times 10^{13}$ | $2.1 \times 10^{9}$ | 38 |
| 95 521 | 20 | 40.3 | 15 Ta | $1.1 \times 10^{13}$ | $4.0 \times 10^{9}$ | 35 |
| 95 522 | 27 | 0.3 | 15 Ta | $3.8 \times 10^{12}$ | $1.2 \times 10^{9}$ | 45 |
| 95 523 | 27 | 39.6 | 15 Ta | $4.2 \times 10^{12}$ | $7.1 \times 10^{8}$ | 40 |
| 95 524 | 27 | 76.6 | 15 Ta | $2.6 \times 10^{12}$ | $6.5 \times 10^{8}$ | 39 |
| 97 381 | 20 | 0 | 15 Ta | $1.6 \times 10^{13}$ | $3.6 \times 10^{9}$ | 90 |
| 97 384 | 20 | 0 | 15 Ta | $2.0 \times 10^{13}$ | $4.3 \times 10^{9}$ | 44 |
| 97 385 | 20 | 80 | 15 Ta | $1.5 \times 10^{13}$ | $3.6 \times 10^{9}$ | 31 |
| 97 386 | 20 | 40 | 15 Ta | $1.2 \times 10^{13}$ | $3.0 \times 10^{9}$ | 41 |
| 97 387 | 20 | 0 | 15 Ta | $2.1 \times 10^{13}$ | $3.8 \times 10^{9}$ | 52 |
| 97 388 | 20 | 80 | 15 Ta | $1.3 \times 10^{13}$ | $2.6 \times 10^{9}$ | 39 |

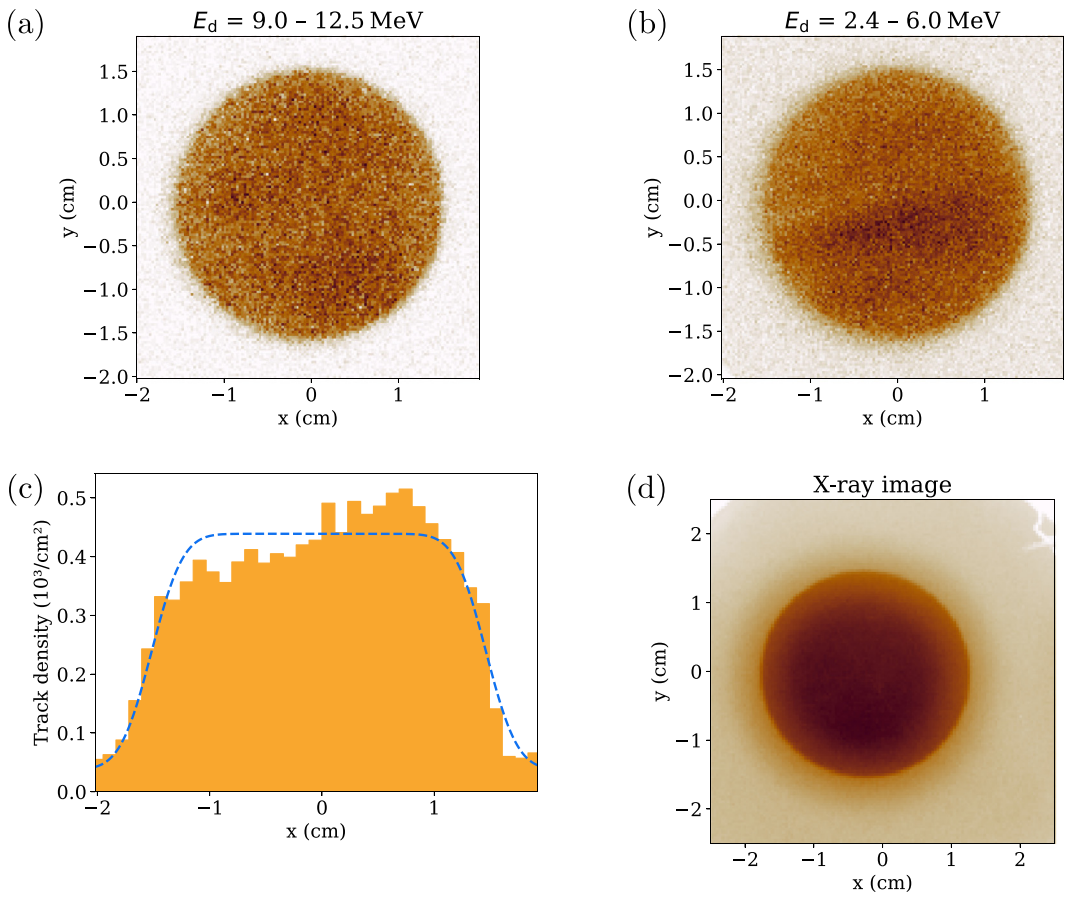


**FIG. 8.** Obtained KODI penumbral images for OMEGA shot number 95 520 (see Table I), view 1. (a) Deuterons above 9 MeV. (b) Deuterons under 6 MeV. (c) Radial histogram of the low-energy deuteron image, along with a fit to an ideal penumbral shape. The fit fails to capture the fluence variations in the center of the image. (d) X-rays imaged by the image plate behind the CR-39.

reconstructions shown in this paper use a termination condition based on the principle of maximum entropy.[34] Each iteration, the posterior probability $\mathcal{P}$ for the reconstructed source, defined as a combination of the likelihood and the entropy as described by Petrovici *et al.*,[34] is computed and saved,

$$\mathcal{P} = \mathcal{L}\exp(\alpha \mathcal{S}), \tag{3}$$

$$\mathcal{S} \equiv -\sum_{k=1}^{m} \frac{G_k}{\sum_{l=0}^{m} G_l} \ln \frac{G_k}{\sum_{l=0}^{m} G_l}, \tag{4}$$

where $\alpha$ is a parameter chosen by the user. While the algorithm does not maximize $\mathcal{P}$, which would be more computationally complex than maximizing $\mathcal{L}$, tracking $\mathcal{P}$ provides a means to discriminate good fits from overfits on the path toward maximum $\mathcal{L}$. Once $\mathcal{P}$ decreases too many iterations in a row, the reconstruction routine returns the vector $\{G_k\}$ corresponding to the highest achieved value of $\mathcal{P}$. This termination condition requires a choice of $\alpha$, which is difficult to select theoretically. However, this termination condition is much less sensitive to $\alpha$ than GKP's condition is to $\chi^2_P$, and a value of $\alpha = 10^2 \frac{1}{n}\sum_{j=1}^{n} F_j$ has been found to work well for a variety of data.

Understanding the accuracy and limitations of the GKP algorithm is a critical prerequisite for accurately using KODI to make inferences about 3D implosion geometry. To this end, it was tested on numerous synthetic images. The GKP algorithm creates reconstructions that generally reproduce the size and shape of synthetic source distributions but appear blurry due to statistical noise, causing small features of the sources to be lost (see Fig. 9). The size of the smallest details that are retained depends on the aperture configuration and yield. This inherent limitation sets the resolution of the instrument.

To quantify the impact of statistics on spatial resolution, synthetic penumbral images were generated at a variety of yields and reconstructed, as shown in Figs. 10(a) and 10(b), and the spatial resolutions of the reconstructions were quantified as shown in Fig. 10(c). By fitting the resolution to a function of the number of tracks in the penumbra, the following relation was obtained:

$$\frac{r_{res}}{r_S} \approx 29 N_P^{-0.35}, \tag{5}$$

where $N_P$ is the number of tracks in the penumbra and given by

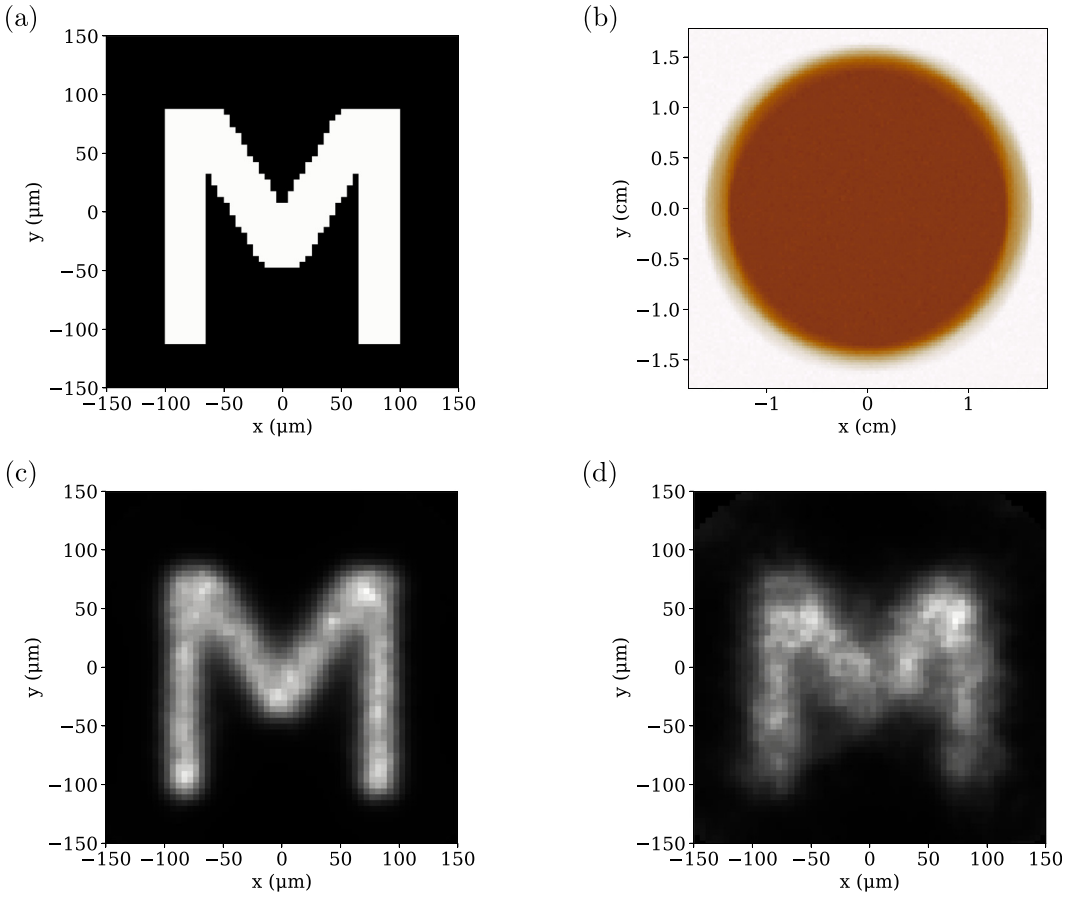


**FIG. 9.** Synthetic KODI images from a hypothetical source in the form of the letter "M." These images can be effectively reconstructed using the GKP algorithm. (a) Knock-on deuteron source. (b) The synthetic KODI image was generated from the source assuming a total deuteron yield of $1 \times 10^{12}$. (c) A GKP reconstruction was performed based on the synthetic KODI image. The reconstruction appears blurry because of the instrument's finite resolution, which is limited only by statistics in this case. Statistical noise in the KODI image also leads to random bright and dim spots throughout the image. However, the overall shape of the letter is reproduced legibly. (d) A GKP reconstruction was performed based on a different synthetic KODI image assuming a yield of $1 \times 10^{10}$. At this yield level, the resolution is impaired, and the reconstruction is less recognizable.

$$N_{\mathrm{P}} = \frac{Y}{8\pi M^2 L^2} \cdot 4\pi N_{\mathrm{A}} M r_{\mathrm{A}} (M-1) r_{\mathrm{S}}, \tag{6}$$

where $N_{\mathrm{A}}$ is the number of apertures, $L$ is the aperture distance from TCC, $r_{\mathrm{S}}$ is the deuteron source size, and $Y$ is the total deuteron yield. This relation is plotted in Fig. 10(d). At values relevant to the commissioning experiment data ($M = 15$, $r_{\mathrm{A}} = 1\,\mathrm{mm}$, $N_{\mathrm{A}} = 1$, $L = 4.2\,\mathrm{cm}$, $r_{\mathrm{S}} = 50\,\mu\mathrm{m}$, $Y = 10^{10}$), the resolution is 23 $\mu$m. This is sufficient to diagnose P1 and P2 asymmetries. The resolution can be improved by using an array of multiple apertures,[35] or by moving the aperture closer to the implosion.

### A. Aperture charging

One common challenge in charged-particle penumbral imaging is that of aperture charging.[36,37] If the aperture accumulates a negative electric charge before particles pass through it, the point-spread function will be distorted. Specifically, the intensity from near the edge of the image will be depleted outward, causing the image to appear larger, the penumbra to appear wider, and the image to appear peaked in the center rather than uniform. These distortions are particularly apparent in the KODI commissioning data described in Sec. III. Therefore, a model of the distortions is needed to account for this effect in the analysis when it cannot be eliminated in the experimental setup.

For an azimuthally symmetric aperture, the electric field experienced by the deuterons is radial and given by a two-dimensional function $\vec{\mathcal{E}}(r,z)$. The displacement of deuterons passing through the aperture depends on the path-integral of that function along the deuteron's trajectory $(r(l), z(l))$. Assuming the field is strongly peaked in the aperture plane where $z = L$, and the deuterons' paths are nearly parallel to the aperture axis (i.e., $L \gg r_{\mathrm{A}}$) that path integral is expressed as

$$\int_{-\infty}^{\infty} \vec{\mathcal{E}}(r(l), z(l))\mathrm{d}l \approx \mathcal{E}_r(r_{\mathrm{P}}, L)\,\hat{r}\,\delta, \tag{7}$$

$$\mathcal{E}_r(r_{\mathrm{P}}, L) = \frac{\sigma}{2\pi\epsilon_0} \int_{-r_{\mathrm{A}}}^{r_{\mathrm{A}}} \frac{\mathrm{d}y}{r_{\mathrm{P}} - y} \frac{\sqrt{r_{\mathrm{A}}^2 - y^2}}{\sqrt{r_{\mathrm{P}}^2 - 2r_{\mathrm{P}}y + r_{\mathrm{A}}^2}}, \tag{8}$$

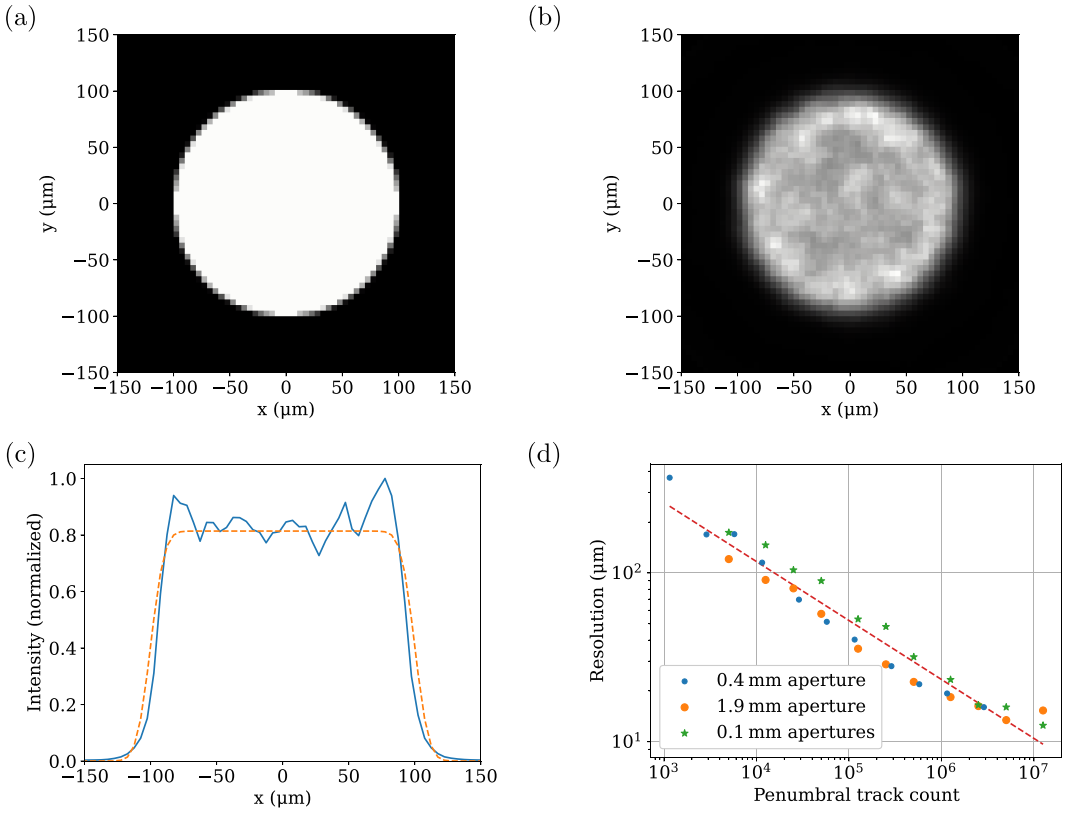


**FIG. 10.** KODI spatial resolution as a function of yield for a variety of aperture configurations. (a) A synthetic deuteron source shaped like a 100 $\mu$m radius disk of uniform intensity with a sharp edge. (b) A GKP reconstruction based on the synthetic KODI image generated from the synthetic source assuming a total deuteron yield of $1 \times 10^{12}$. (c) Lineout across the reconstruction. A boxcar function convolved with a Gaussian was fit to the lineout to quantify the spatial resolution of the reconstruction. In this case, a Gaussian with a width of 19.5 $\mu$m best fits the result, which means the resolution of this reconstruction is 19.5 $\mu$m. (d) Spatial resolution as a function of track count in the penumbra, as defined by Eq. (6). The images were synthetically produced assuming three different aperture configurations: a single aperture 400 $\mu$m in diameter, a single aperture 1900 $\mu$m in diameter, and nineteen apertures 100 $\mu$m in diameter. All three used an aperture distance of 4.2 cm and a magnification of 15. Equation (5) approximately predicts the resolution for all three configurations, though there is some remaining variation between them.

where $\sigma$ is the areal charge density of the aperture, $r_A$ is the radius of the aperture, and $r_{\mathcal{P}}$ is the distance between the point where the particle crosses the aperture plane and the center of the aperture. $\delta$ is an arbitrary length scale that can be set along with $\sigma$ to fit the data. This integral is solved numerically to build a map of the electric field inside the aperture, though one must take care to eliminate the pole where $y = r_P$.

In this limit, the only effect of the electric field is a radial impulse instantaneously imparted on each deuteron as it passes through the aperture. The resulting radial displacement of the deuteron is calculated and used to solve for the modified point-spread function,

$$r_D \approx M r_P + \frac{1}{2}\frac{eL}{E_d}\mathcal{E}_r(r_P, L)\,\delta, \tag{9}$$

$$P_{ik} \propto \frac{M^2 r_P}{r_D}\left(\frac{\partial r_D}{\partial r_P}\right)^{-1}. \tag{10}$$

Here, $r_D$ is the radial position of the particle when it strikes the detector, and $E_d$ is the energy of the deuteron.

This model predicts a broad, round shoulder just inside the penumbra, as well as a broadening of the penumbra, in agreement with the observations. A comparison of this model to data from the commissioning experiments is seen in Fig. 11. In the case shown in Fig. 11(a), this model explains the shape of the data accurately. In the case shown in Fig. 11(b), there still exist systematic differences between the best fit and actual radial profile—it overestimates the track-density in the shoulder and underestimates it in the center. The causes of these discrepancies are not fully understood, but often correspond to non-radially symmetric density variations in the center of the image, which cannot be explained by this electric field model. In all cases, the model explains the shape of the penumbral image better than is possible without aperture charging.

Using this modified point-spread function when reconstructing data from the commissioning experiments has a substantial effect on the result; the sources reconstructed naively are 2–5 times larger in radius than those reconstructed with the charging model. This poses a major challenge for KODI data analysis, and as such efforts are under way to mitigate charging in future KODI experiments. For existing data, however, the described model seems to be sufficient to compensate for the effect, as the sizes of resulting reconstructions agree well with simulations, as further discussed in Sec. V.

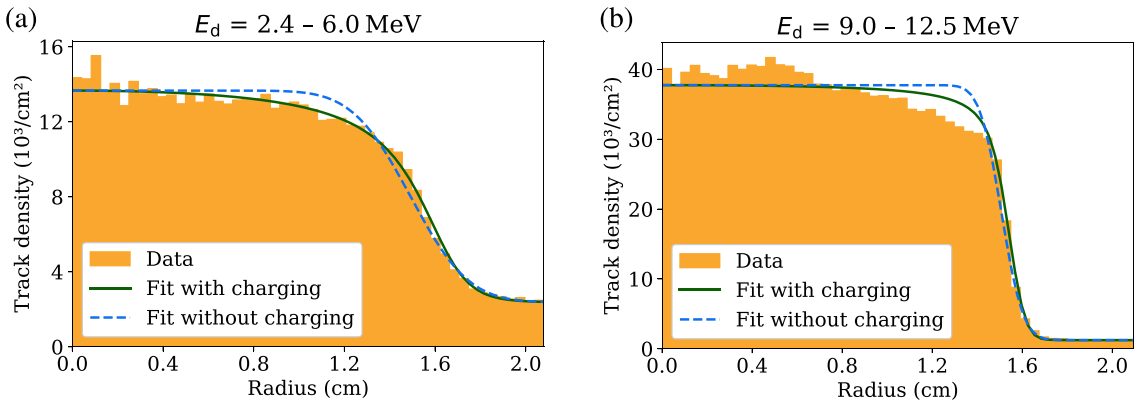


**FIG. 11.** Radial-track-density profiles for two experimentally obtained penumbral deuteron images. (a) Radial-track-density profile for low-energy deuterons on shot 95 524. It displays a rounded "shoulder" region just inside the penumbra, which cannot be described assuming an ideal aperture (dashed line), but is described accurately by including the aperture charging model presented here when setting $\sigma\delta/(4\pi\epsilon_0) = 9.08$ kV (solid line). (b) Radial-track-density profile for high-energy deuterons on shot 95 521. While a best fit can be reached by setting $\sigma\delta/(4\pi\epsilon_0) = 7.37$ kV, the aperture charging model is insufficient to describe some features, such as the spike in track-density seen near the center, which is due to non-radially symmetric track-density variations.

## V. EXPERIMENTAL RESULTS

Reconstructions of deuteron sources were made from each of the penumbral images measured in the commissioning experiment using the GKP algorithm with the aperture charging model. Several images were compromised by data artifacts or mispointing to a degree that prevented adequate reconstruction. Among those that could be reconstructed, the images for deuterons above 9 MeV and for deuterons below 6 MeV were reconstructed separately. Overall, they were all relatively round, with P2 asymmetries ranging from 0% to 15% of the source radius. Measured source radii were fairly consistent between the three lines of sight, with variations of about 15% on each implosion. An example from these reconstructions is shown in Fig. 12.

For comparison, 1D hydrodynamic simulations were performed using the code LILAC,[38] and KODI images were generated based on those simulations using the Monte Carlo particle tracking code IRIS.[39]

The reconstructed high-energy deuteron sources, which are approximately equivalent to neutron sources, are quantified and illustrated in Fig. 13(a). The sources range from 20 to 40 $\mu$m in radius. This agrees well with the LILAC, which predicted high-energy source sizes of about 30 $\mu$m for both shell thicknesses. The source sizes of the thick-shell capsules show more variation, likely owing to the lower deuteron yields provided by the thick-shell capsules and the correspondingly greater uncertainty in reconstructions of their source sizes.

The reconstructed low-energy deuteron sources, shown in Fig. 13(b), are significantly larger, ranging from 50 to 80 $\mu$m. This is also reasonable, since the low-energy knock-on deuteron source extends into the dense shell that surrounds the hot-spot at bang time. Unlike the high-energy sources, the low-energy source sizes correlate with implosion shell thickness; the low-energy source for the thick-shell capsules are systematically about 15 $\mu$m larger than for the thin-shell capsules, reflecting a thicker shell at bang time. This corresponds to a larger average shell radius, which explains why the thick-shell capsules had about the same measured $\rho R$ as the thin-shell ones (38 and 41 mg/cm$^2$, respectively) despite the greater shell mass. Again, this is in good agreement with LILAC, which predicted a low-energy deuteron source size of 60 $\mu$m for the thin-shell capsules and 75 $\mu$m for the thick-shell capsules.

Because the high- and low-energy deuteron images were recorded on the same detector, the absolute offset between their centroids could be measured. This separation was found to correlate with the prescribed offset of the target from TCC. The high-energy deuteron source consistently appeared further from TCC than the low-energy deuteron source, as shown in Fig. 14. This suggests a P1 asymmetry in the shell at bang time that increases the thickness on the side nearest TCC, which is exactly what has been predicted by 3D hydrodynamic simulations of offset cryogenic implosions.[40] This indicates that KODI can reliably measure P1 asymmetries.

Simulations predict that such asymmetries are accompanied by a strong flow away from TCC in the hot spot. The experimental hot-spot velocity was measured by nTOF spectrometers,[14] but as there were only two shots where both KODI and the nTOFs provided usable data, judging correlations is difficult. However, the measured flow in those two cases had a direction similar to both the offset (within 36°) and the deuteron source separation (within 55°), as expected.

Finally, x-ray sources were also imaged in these commissioning experiments. They range from 20 to 50 $\mu$m in radius. The x-ray source is similar in extent to the hot-spot as probed by high-energy deuterons, as shown in Fig. 15(a), but correlates with the extent of the shell as probed by low-energy deuterons, as shown in Fig. 15(b). The thick-shell implosions' x-ray sources were about 15 $\mu$m larger than the thin-shell implosions'. This suggests a high electron temperature in the dense shell region, allowing it to contribute a significant amount of x-ray emission. This does not agree with LILAC,[41,47] which predicted the x-ray source sizes to be uncorrelated with shell extent.

It is possible that the electron temperature profiles are broadened near the hot-spot/shell interface by mixing effects, which LILAC does not account for. The shell in these shots contains carbon and is several times denser than the hot-spot, so a modest increase in temperature due to non-hydrodynamic effects could explain the significant increase in emission. A shell-fuel mix width of 11 $\mu$m has been previously

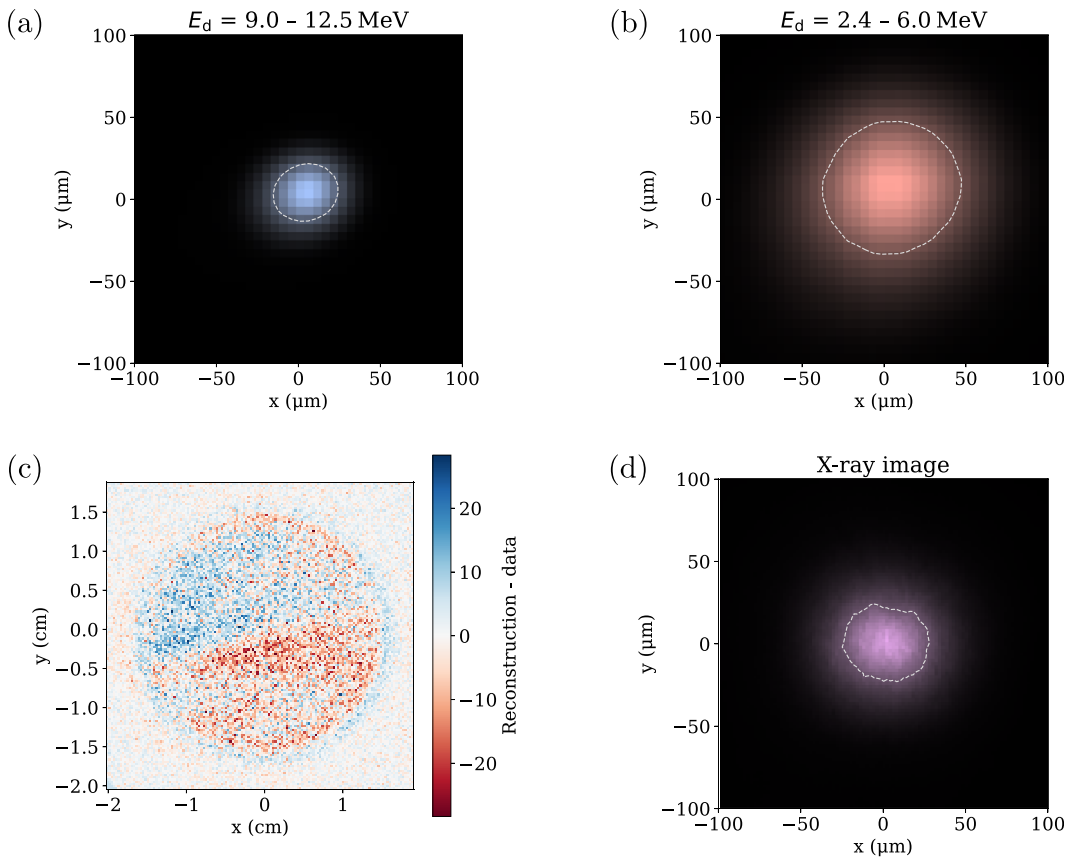


**FIG. 12.** Reconstructed deuteron sources for OMEGA shot number 95 520 (see Table I), view 1, corresponding to the penumbral images shown in Fig. 8. (a) The reconstructed source for deuterons over 9 MeV, exhibiting a P2 asymmetry whose magnitude is 9.5% of the radius. (b) The reconstructed source for deuterons under 6 MeV, exhibiting a P2 asymmetry of 3.5%, in a similar direction. (c) The residuals from the reconstruction of the low-energy deuteron source. There remain substantial errors in the center of the image due to non-radial variations that are not accounted for by the model. However, the penumbra is accurately matched by the reconstruction. (d) The reconstructed x-ray source, exhibiting a P2 asymmetry of 8.1%.

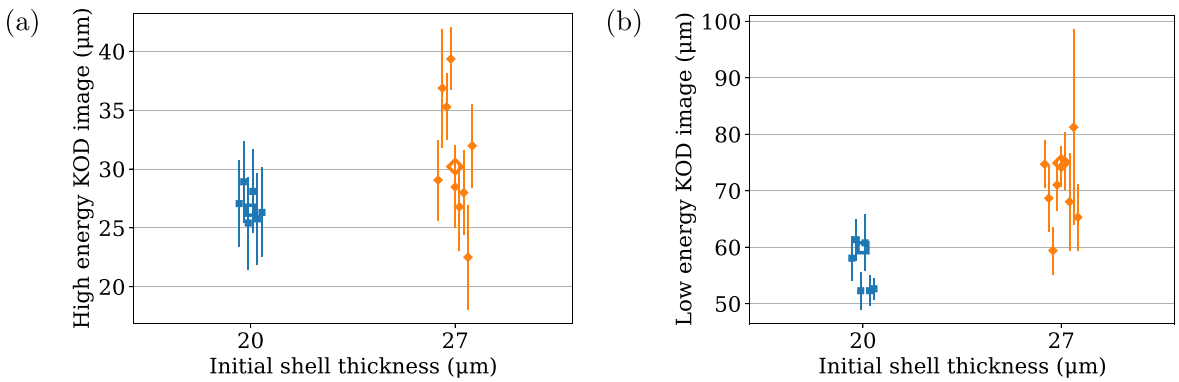


**FIG. 13.** (a) The radii of the reconstructed high-energy deuteron source and (b) low-energy deuteron source for two different capsule-shell thicknesses used in the commissioning experiments. The high-energy deuteron data represent the hot-spot, and the low-energy data represent the extent of the surrounding shell. These values were quantified using the azimuthally averaged radius of the 50% contour. The solid points indicate measurements from the experiments while the hollow points indicate 1D hydrodynamic simulations. Some horizontal jitter has been added to make the data more visible.

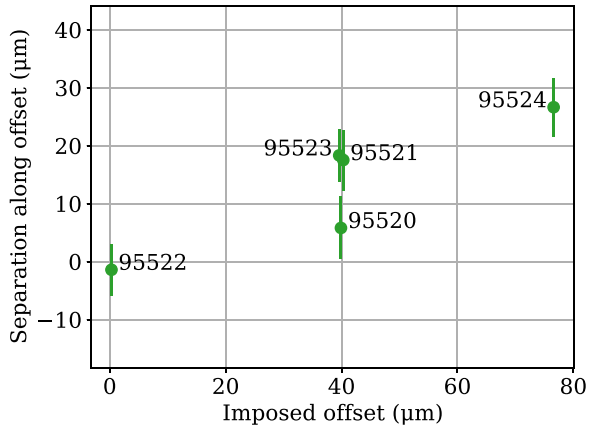


**FIG. 14.** The measured separation between the high- and low-energy reconstructed deuteron source centroids as a function of prescribed offset. The separation between the sources was measured with KODI on three lines of sight, projected into 3D, and then projected onto the axis along which the capsule was offset from TCC. The sign of the projected separation is defined such that it is positive when the low-energy source is closer to TCC than the high-energy source, and negative when the high-energy source is closer. Only five of the twelve shots are shown here, because only five had usable data on all three lines of sight and in both energy bins, as is necessary to reconstruct the separation in 3D.

measured in similar implosions,[42] so 15 $\mu$m of mix, as needed to explain these data, is plausible. Additional hypotheses to explain this discrepancy will be explored in the future. This effect would not necessarily be evident in most cryo implosions where the dense shell around the hot spot is DT rather than CD, because of DT's lower $Z$.

## VI. CONCLUSIONS AND PATH FORWARD

The first KODI proof-of-principle commissioning experiments have been conducted successfully. Analysis techniques have been developed to reconstruct 2D knock-on deuteron sources from the commissioning data. The reconstructed source sizes agree with simulations, and reconstructed P1 asymmetries correlate with the prescribed capsule offsets. This indicates that the KODI technique provides high-fidelity data of the shell morphology.

More work is required to ensure the principles behind it are well-understood and that the diagnostic is implemented to its full potential. The reconstruction techniques must continue to be evaluated at different yield levels and aperture configurations using synthetic data. Eventually, images from multiple lines of sight must be combined to infer the 3D morphology of the hot-spot and surrounding high-density shell. This 3D reconstruction problem is analogous to the combination of neutron images obtained along multiple different lines of sight, as is currently done at the NIF.[21] However, the stopping of knock-on deuterons as they traverse the high-density shell, which is not present in neutron images, complicates the analysis. 3D reconstruction algorithms that account for this effect are currently being developed for KODI data.

New extensions to knock-on deuteron image analysis are also being investigated. For example, to address the presence of knock-on tritons in KODI images, a technique to discriminate different particle species by etching CR-39 multiple times is being considered. In addition, alternative penumbral aperture configurations are being implemented to achieve better efficiency and spatial resolution. Recent cryogenic shots have been executed with hexagonal arrays of many circular apertures, increasing the number of tracks in the penumbra twelve-fold [and thus improving the resolution by a factor of 2.4 as per Eq. (5)]. Finally, alternative materials for the aperture and surrounding hardware are being designed and tested with the aim of reducing the effect of aperture charging. Ultimately, these techniques will allow more accurate reconstruction of the hot-spot and fuel morphology at stagnation.

Going forward, experiments over the next year will be used to further test and validate the new KODI hardware and techniques to address the challenges listed above. The number of cryogenic DT physics experiments will gradually increase throughout the next phase of the project, as this capability is considered absolutely essential to the ICF program at OMEGA.

## VII. SUMMARY

Mitigating the presence of low-mode asymmetries in an ICF implosion is critical for optimizing its performance. Although shell $\rho R$

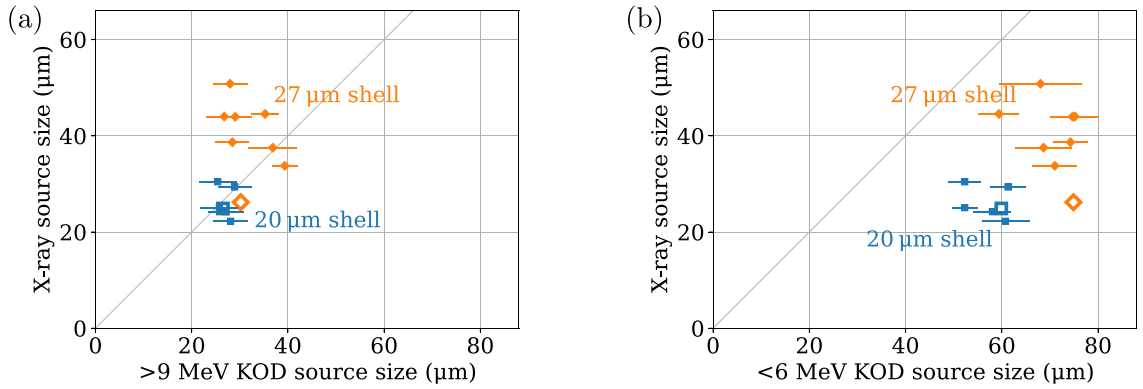


**FIG. 15.** X-ray source radii as a function of the reconstructed deuteron source radii. The solid points indicate measurements from the experiments while the hollow points indicate 1D hydrodynamic simulations. (a) A comparison of x-ray and high-energy deuteron source radii. If x-ray emission were dominated by the hot-spot, the source sizes would be nearly identical. In reality, while they are similar for the thin-shell implosions, the x-ray source is significantly larger than the hot-spot for the thick-shell implosions. (b) A comparison of x-ray and low-energy deuteron source radii. There is a positive correlation between them, indicating that the dense shell contributes significantly to the x-ray emission.

asymmetries are known to be detrimental to the implosion performance, no methods currently exist to diagnose them in detail at the OMEGA laser facility.

KODI is a new diagnostic technique that will allow for imaging of the 3D morphology of ICF implosions by taking advantage of the kinematics of knock-on deuterons. It comprises penumbral imagers along three nearly orthogonal lines of sight of an implosion. KODI has been implemented and successfully fielded in commissioning experiments where the first KODI images were obtained. 2D reconstructions of these images reveals that the hot-spot and shell radii were accurately predicted by 1D hydro simulations, and that a P1 asymmetry was consistently present and correlated with the prescribed capsule offsets.

Analysis techniques to reconstruct the full 3D morphology of the implosion are currently in development, as are several extensions to the KODI technique that will ultimately improve the accuracy and resolution of the instrument.

More experiments are planned for the next year, in which KODI will provide information about the 3D morphology of ICF implosions hitherto unavailable. This information will be used to study the origin and impact of low-mode asymmetries on implosion performance at a level of detail never before achievable at OMEGA.

## ACKNOWLEDGMENTS

This work was supported in part by the U.S. Department of Energy NNSA MIT Center-of-Excellence under Contract No. DE-NA0003868.

## AUTHOR DECLARATIONS

### Conflict of Interest

The authors have no conflicts to disclose.

### Author Contributions

**Justin Haruaki Kunimune:** Investigation (equal); Writing – original draft (lead); Writing – review and editing (equal). **Benjamin Bachmann:** Supervision (equal). **Johan A Frenje:** Investigation (equal); Supervision (equal); Writing – review and editing (equal). **Hans George Rinderknecht:** Investigation (equal); Writing – review and editing (equal). **Patrick Adrian:** Investigation (equal); Writing – review and editing (equal). **Peter Ver Bryck Heuer:** Investigation (equal); Writing – review and editing (equal). **Sean Patrick Regan:** Supervision (equal). **Fredrick H. Seguin:** Investigation (equal). **Maria Gatu Johnson:** Investigation (equal). **Radha Bahukutumbi:** Investigation (equal). **James P. Knauer:** Supervision (equal).

## DATA AVAILABILITY

The data that support the findings of this study are available from the corresponding author upon reasonable request.

## REFERENCES

[1]S. Atzeni and J. Meyer-ter Vehn, *The Physics of Inertial Fusion: Beam-Plasma Interaction, Hydrodynamics, Hot Dense Matter* (Oxford Science Publications, Clarendon Press, Oxford, 2004).
[2]R. L. McCrory, J. M. Soures, C. P. Verdo, F. J. Marshall, S. A. Letzring, S. Skupsky, T. J. Kessler, R. L. Kremens, K. P. Knauer, H. Kim, J. Delettrez, R. L. Keck, and D. K. Bradley, Nature **335**, 225–229 (1988).
[3]A. B. Zylstra, O. A. Hurricane, D. A. Callahan, A. L. Kritcher, J. E. Ralph, H. F. Robey, J. S. Ross, C. V. Young, K. L. Baker, D. T. Casey, T. Döppner, L. Divol, M. Hohenberger et al., Nature **601**, 542–548 (2022).
[4]E. L. Dewald, O. L. Landen, J. Salmonson, L. Masse, M. Tabak, V. A. Smalyuk, S. Schiaffino, R. Heredia, M. Schneider, and A. Nikroo, Phys. Plasmas **27**, 122703 (2020).
[5]O. M. Mannion, I. V. Igumenshchev, K. S. Anderson, R. Betti, E. M. Campbell, D. Cao, C. J. Forrest, M. G. Johnson, V. Y. Glebov, V. N. Goncharov, V. Gopalaswamy, S. T. Ivancic, D. W. Jacobs-Perkins, A. Kalb, J. P. Knauer, J. Kwiatkowski, A. Lees, F. J. Marshall, M. Michalko, Z. L. Mohamed, D. Patel, H. G. Rinderknecht, R. C. Shah, C. Stoeckl, W. Theobald, K. M. Woo, and S. P. Regan, Phys. Plasmas **28**, 042701 (2021).
[6]D. T. Casey, B. J. MacGowan, J. D. Sater, A. B. Zylstra, O. L. Landen, J. Milovich, O. A. Hurricane, A. L. Kritcher, M. Hohenberger, K. Baker, S. L. Pape, T. Döppner, C. Weber, H. Huang, C. Kong, J. Biener, C. V. Young, S. Haan, R. C. Nora, S. Ross, H. Robey, M. Stadermann, A. Nikroo, D. A. Callahan, R. M. Bionta, K. D. Hahn, A. S. Moore, D. Schlossberg, M. Bruhn, K. Sequoia, N. Rice, M. Farrell, and C. Wild, Phys. Rev. Lett. **126**, 025002 (2021).
[7]M. Gatu Johnson, P. J. Adrian, K. S. Anderson, B. D. Appelbe, J. P. Chittenden, A. J. Crilly, D. Edgell, C. J. Forrest, J. A. Frenje, V. Y. Glebov, B. M. Haines, I. Igumenshchev, D. Jacobs-Perkins, R. Janezic, N. V. Kabadi, J. P. Knauer, B. Lahmann, O. M. Mannion, F. J. Marshall, T. Michel, F. H. Séguin, R. Shah, C. Stoeckl, C. A. Walsh, and R. D. Petrasso, Phys. Plasmas **27**, 032704 (2020).
[8]I. V. Igumenshchev, D. T. Michel, R. C. Shah, E. M. Campbell, R. Epstein, C. J. Forrest, V. Y. Glebov, V. N. Goncharov, J. P. Knauer, F. J. Marshall, R. L. McCrory, S. P. Regan, T. C. Sangster, C. Stoeckl, A. J. Schmitt, and S. Obenschain, Phys. Plasmas **24**, 056307 (2017).
[9]M. Gatu Johnson, B. D. Appelbe, J. P. Chittenden, J. Delettrez, C. Forrest, J. A. Frenje, V. Y. Glebov, W. Grimble, B. M. Haines, I. Igumenshchev, R. Janezic, J. P. Knauer, B. Lahmann, F. J. Marshall, T. Michel, F. H. Séguin, C. Stoeckl, C. Walsh, A. B. Zylstra, and R. D. Petrasso, Phys. Rev. E **98**, 051201 (2018).
[10]O. A. Hurricane, D. T. Casey, O. Landen, A. L. Kritcher, R. Nora, P. K. Patel, J. A. Gaffney, K. D. Humbird, J. E. Field, M. K. G. Kruse, J. L. Peterson, and B. K. Spears, Phys. Plasmas **27**, 062704 (2020).
[11]O. A. Hurricane, D. T. Casey, O. Landen, D. A. Callahan, R. Bionta, S. Haan, A. L. Kritcher, R. Nora, P. K. Patel, P. T. Springer, and A. Zylstra, Phys. Plasmas **29**, 012703 (2022).
[12]A. K. Davis, D. T. Michel, R. S. Craxton, R. Epstein, M. Hohenberger, T. Mo, and D. H. Froula, Rev. Sci. Instrum. **87**, 11E340 (2016).
[13]P. Adrian, J. Frenje, N. Kabadi, M. Gatu Johnson, A. Bose, B. Lahmann, J. Pearcy, G. D. Sutcliffe, T. Johnson, F. H. Séguin, C. K. Li, R. D. Petrasso, R. Shah, O. Mannion, C. Sorce, V. Glebov, S. Regan, Z. Mohamed, H. G. Rinderknecht, B. Bachmann, H. Sio, B. Aguirre, W. Martin, B. Scheiner, and M. Schmitt, Rev. Sci. Instrum. **92**, 043548 (2021).
[14]R. A. Lerche, V. Y. Glebov, M. J. Moran, J. M. McNaney, J. D. Kilkenny, M. J. Eckart, R. A. Zacharias, J. J. Haslam, T. J. Clancy, M. F. Yeoman, D. P. Warwas, T. C. Sangster, C. Stoeckl, J. P. Knauer, and C. J. Horsfield, Rev. Sci. Instrum. **81**, 10D319 (2010).
[15]J. A. Frenje, Plasma Phys. Controlled Fusion **62**, 023001 (2020).
[16]F. H. Séguin, J. A. Frenje, C. K. Li, D. G. Hicks, S. Kurebayashi, J. R. Rygg, B.-E. Schwartz, R. D. Petrasso, S. Roberts, J. M. Soures, D. D. Meyerhofer, T. C. Sangster, J. P. Knauer, C. Sorce, V. Y. Glebov, C. Stoeckl, T. W. Phillips, R. J. Leeper, K. Fletcher, and S. Padalino, Rev. Sci. Instrum. **74**, 975 (2003).
[17]J. A. Frenje, C. K. Li, F. H. Séguin, S. Kurebayashi, R. D. Petrasso, J. M. Soures, J. Delettrez, V. Y. Glebov, D. D. Meyerhofre, P. B. Radha, S. Roberts, T. C. Sangstre, S. Skupsky, and C. Stoeckl, Phys. Plasmas **9**, 4719 (2002).
[18]J. A. Frenje, C. K. Li, F. H. Séguin, D. T. Casey, R. D. Petrasso, T. C. Sangstre, R. Betti, V. Y. Glebov, and D. D. Meyerhofre, Phys. Plasmas **16**, 042704 (2009).
[19]G. H. Miller, E. I. Moses, and C. R. Wuest, Nucl. Fusion **44**, S228–S238 (2004).
[20]J. R. Root, D. R. Jedlovec, E. R. Edwards, C. B. Yeamans, T. Golod, J. Hernandez, P. Adams, and G. Brunton, "Development of the real-time neutron activation diagnostic system for NIF," Proc. SPIE **10390**, 46–51 (2017).
[21]P. L. Volegov, S. H. Batha, V. Geppert-Kleinrath, C. R. Danly, F. E. Merrill, C. H. Wilde, D. C. Wilson, D. T. Casey, D. Fittinghoff, B. Appelbe, J. P. Chittenden, A. J. Crilly, and K. McGlinchey, J. Appl. Phys. **127**, 083301 (2020).
[22]K. Nugent and B. Luther-Davies, Opt. Commun. **49**, 393 (1984).

[23]F. H. Séguin, J. L. DeCiantis, J. A. Frenje, S. Kurebayashi, C. K. Li, J. R. Rygg, C. Chen, V. Berube, B. E. Schwartz, R. D. Petrasso, V. A. Smalyuk, F. J. Marshall, J. P. Knauer, J. A. Delettrez, P. W. McKenty, D. D. Meyerhofer, S. Roberts, T. C. Sangster, K. Mikaelian, and H. S. Park, Rev. Sci. Instrum. **75**, 3520 (2004).
[24]F. H. Séguin, C. K. Li, J. L. DeCiantis, J. A. Frenje, J. R. Rygg, R. D. Petrasso, F. J. Marshall, V. Smalyuk, V. Y. Glebov, J. P. Knaure, T. C. Sangstre, J. D. Kilkenny, and A. Nikroo, Phys. Plasmas **23**, 032705 (2016).
[25]A. Fews, M. Lamb, and M. Savage, Opt. Commun. **94**, 259 (1992).
[26]A. Fews, Nucl. Instrum. Methods Phys. Res. B **71**, 465 (1992).
[27]T. W. Phillips, M. D. Cable, D. G. Hicks, C. K. Li, R. D. Petrasso, and F. H. Seguin, Rev. Sci. Instrum. **68**, 596 (1997).
[28]B. Lahmann, M. Gatu Johnson, J. A. Frenje, Y. Y. Glebov, H. G. Rinderknecht, F. H. Séguin, G. Sutcliffe, and R. D. Petrasso, Rev. Sci. Instrum. **91**, 053502 (2020).
[29]J. A. Frenje, C. K. Li, F. H. Séguin, D. G. Hicks, S. Kurebayashi, R. D. Petrasso, S. Roberts, V. Y. Glebov, D. D. Meyerhofer, T. C. Sangster, J. M. Soures, C. Stoeckl, C. Chiritescu, G. J. Schmid, and R. A. Lerche, Rev. Sci. Instrum. **73**, 2597 (2002).
[30]D. Ress, R. A. Lerche, R. J. Ellis, S. M. Lane, and K. A. Nugent, Science **241**, 956 (1988).
[31]S. Nozaki, Y.-W. Chen, Z. Nakao, R. Kodama, and H. Shiraga, Rev. Sci. Instrum. **74**, 2240 (2003).
[32]The simplest reconstruction techniques are direct methods like Wiener Filters,[30] deconvolutions,[22,47] and back-projections.[23,44] However, such techniques are designed for applications with high signal levels, and applying them to KODI data results in an unacceptably high noise level in the reconstructed image. Stochastic heuristic methods such as simulated annealing are more robust to input noise,[31,35] but are complicated and computationally expensive.
[33]V. I. Gelfgat, E. L. Kosarev, and E. R. Podolyak, Comput. Phys. Commun. **74**, 335 (1993).
[34]M. A. Petrovici, C. Damian, and D. Coltuc, Adv. Electr. Comput. Eng. **18**, 77 (2018).
[35]T. Ueda, S. Fujioka, S. Nozaki, R. Azuma, D.-W. Chen, and H. Nishimura, Rev. Sci. Instrum. **81**, 073505 (2010).
[36]J. L. DeCiantis, F. H. Séguin, J. A. Frenje, V. Berube, M. J. Canavan, C. D. Chen, S. Kurebayashi, C. K. Li, J. R. Rygg, B. E. Schwartz, R. D. Petrasso, J. A. Delettrez, S. P. Regan, V. A. Smalyuk, J. P. Knauer, F. J. Marshall, D. D. Meyerhofer, S. Roberts, T. C. Sangster, C. Stoeckl, K. Mikaelian, H. S. Park, and H. F. Robey, Rev. Sci. Instrum. **77**, 043503 (2006).
[37]H. G. Rinderknecht, "Studies of non-hydrodynamic processes in ICF implosions on OMEGA and the national ignition facility," Ph.D. thesis (Massachusetts Institute of Technology, Cambridge, 2015).
[38]J. Delettrez, R. Epstein, M. C. Richardson, P. A. Jaanimagi, and B. L. Henke, Phys. Rev. A **36**, 3926 (1987).
[39]P. B. Radha, V. Yu. Glebov, D. D. Meyerhofer, C. Stoeckl, J. M. Soures, C. K. Li, R. D. Petrasso, and F. H. Séguin, "A consistent measurement-based picture of core-mix in direct-drive implosions on OMEGA," Technical Report No. DOE/SF/19460-393, Laboratory for Laser Energetics, 2001.
[40]I. V. Igumenshchev, V. N. Goncharov, F. J. Marshall, J. P. Knauer, E. M. Campbell, C. J. Forrest, D. H. Froula, V. Y. Glebov, R. L. McCrory, S. P. Regan, T. C. Sangster, S. Skupsky, and C. Stoeckl, Phys. Plasmas **23**, 052702 (2016).
[41]X-ray images generated from the LILAC simulations were based on the spatially resolved bremsstrahlung spectrum, and accounted for attenuation in the filtering and in the image plate.[47]
[42]H. M. Johns, R. C. Mancini, T. Nagayama, D. C. Mayes, R. Tommasini, V. A. Smalyuk, S. P. Regan, and J. A. Delettrez, Phys. Plasmas **23**, 012709 (2016).
[43]H. G. Rinderknecht, P. V. Heuer, J. Kunimune, P. J. Adrian, J. P. Knauer, W. Theobald, R. Fairbanks, B. Brannon, L. Ceurvorst, V. Gopalaswamy, C. A. Williams, P. B. Radha, S. P. Regan, M. G. Johnson, F. H. Séguin, and J. A. Frenje, "A Knock-On Deuteron Imager for Measurements of Fuel and Hot-Spot Asymmetry in Direct-Drive Inertial Confinement Fusion Implosions," Rev. Sci. Instrum. (unpublished).
[44]B. Bachmann, A. L. Kritcher, L. R. Benedetti, R. W. Falcone, S. Glenn, J. Hawreliak, N. Izumi, D. Kraus, O. L. Landen, S. L. Pape, T. Ma, F. Pérez, D. Swift, and T. Döppner, Rev. Sci. Instrum. **85**, 11D614 (2014).
[45]L. Disdier, A. Rouyer, D. Wilson, A. Fedotoff, C. Stoeckl, J.-L. Bourgade, V. Glebov, J.-P. Garçonnet, and W. Seka, Nucl. Instrum. Methods Phys. Res., Sect. A **489**, 496 (2002).
[46]D. T. Casey, P. L. Volegov, F. E. Merrill, D. H. Munro, G. P. Grim, O. L. Landen, B. K. Spears, D. N. Fittinghoff, J. E. Field, and V. A. Smalyuk, Rev. Sci. Instrum. **87**, 11E715 (2016).
[47]J. H. Hubbell and S. M. Seltzer, "Tables of x-ray mass attenuation coefficients and mass energy-absorption coefficients 1 keV to 20 MeV for elements Z = 1 to 92 and 48 additional substances of dosimetric interest," Technical Report No. NISTIR 5632, National Institute of Standards and Technology, 1995.